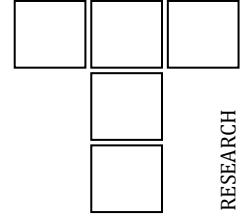




DOI: 10.24874/ti.1742.08.24.12

Tribology in Industry

www.tribology.rs



Dynamic and Thermal Performance Analysis of Textured Bearings with TiO₂ Nanoparticles

Mohanad R. Hameed^{a,*} , Sarmad A. Ali^a 

^aUniversity of Babylon, Institution of Engineering/Al-Musayab, Iraq

Keywords:

Textured journal bearing
Nano lubricant
CFD
Elastic deformation
Stiffness coefficients

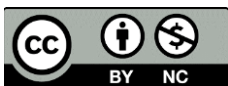
ABSTRACT

This work investigates the merged influences of rectangular surface textures and titanium dioxide nanoparticle additives on the dynamic and thermal characteristics of journal bearings utilising computational fluid dynamics in Fluent software. A fluid-structure interaction approach was applied to account for elastic deformation, while the Zwart–Gerber–Belamri method was employed to simulate cavitation effects. The analysis focused on texture depths ranging from 0.5 to 2.0 and eccentricity ratios between 0.2 and 0.8, examining critical zones of the bearing surface: convergence, divergence, and pressure-increasing regions. Results revealed that an optimal texture depth of 1.0 and an eccentricity ratio of 0.3 in the pressure-increasing zone led to significantly enhanced dynamic and thermal characteristics compared to untextured bearings. Adding nanoparticles further improved performance, achieving levels surpassing textured bearings without additives in the same zone.

* Corresponding author:

Mohanad Ramadhan Hameed
E-mail:
msb.mohanad.ramadhan@uobabylon.edu.iq

Received: 22 August 2024
Revised: 6 September 2024
Accepted: 14 December 2024



© 2025 Published by Faculty of Engineering

1. INTRODUCTION

Dynamic properties such as stiffness and damping are fundamental to ensuring stability and efficiency in journal bearings (JBs), especially in high-speed machinery. These properties directly influence a JB's ability to handle loads, minimise vibrations, and maintain stable performance under varying conditions [1]. Improving these dynamic attributes is crucial for reducing maintenance costs, preventing equipment failures, and optimising overall system performance. In the field of tribology, surface textures have received significant

attention due to their potential to enhance JB's dynamic performance. Surface texturing, achieved by introducing micro-patterns such as grooves, dimples, or micro-cavities onto the bearing surface, has been shown to improve hydrodynamic performance by optimising pressure distribution and increasing lubricant film thickness, thereby enhancing load-bearing capacity and reducing friction.

The role of surface texturing in JB performance has been widely studied, with various configurations and patterns yielding noteworthy improvements. Hamdavi et al. [2] demonstrated

that partial surface texturing on long JBs significantly enhances pressure distribution and load capacity. Tala et al. [3] further showed that strategically positioning textures on the contact surface could notably increase operational efficiency. Kango et al. [4,5] investigated the effects of various surface textures, including micro-cavities, spherical textures, and micro grooving, on the characteristics of JBs. Using numerical methods, they demonstrated that micro-cavities enhance load-bearing capacity and reduce friction, with negative half-wave textures outperforming full-wave designs. Their study also revealed that micro grooving reduces friction and average temperature more effectively than spherical textures, particularly at high eccentricity ratios. Shinde et al. [6] reported improved lubricant pressure and load capacity with partial texturing in conical bearings while reducing the coefficient of friction. Manser et al. [7] investigated the merged effects of surface texturing and journal misalignment, revealing that square, cylindrical, and triangular textures significantly enhance load-bearing capacity and reduce friction, especially in misaligned bearings. Cupillard et al. [8] emphasised that careful texture geometry design improves load capacity and reduces friction, highlighting the importance of texture shape and placement.

Through CFD simulations, Tauviqirrahman et al. [9] examined groove depth, slippage positioning, and eccentricity ratios, discovering that an optimal groove depth, particularly when equal to the minimum film thickness, maximises load support. Additionally, combining slippage and texturing produced further gains in load capacity, especially when strategically placed. Atwal et al. [10] studied hydrodynamic thrust bearings with innovative pad surface designs, such as micro-rectangular pockets and fish scale-inspired textures. They found that this combination significantly enhanced minimum lubricant thickness and decreased friction. Tripathi et al. [11] explored the effects of laser surface texturing on graphite cast iron used in internal combustion engine cylinders, noting that dimples with a pitch of 150 μm and density of 13% minimised friction, while a pitch of 200 μm and 7% density maximised wear resistance.

Partial and varied texturing on JBs has shown additional promise in enhancing stability. Wang et al. [12] studied partial texturing along the

circumferential direction of JBs, finding that dimple depth plays a crucial role in maintaining stability. Singh et al. [13] assessed cylindrical textures' effects on static and dynamic behaviours, utilising the finite element technique to evaluate smooth, fully textured, and partially textured configurations. They concluded that placing textures in the upstream zone with a dimple aspect ratio near 1.0 notably enhances performance. Sharma et al. [14] found that shallow triangular textures improve stiffness and threshold speeds, while deeper textures boost damping properties. Meng et al. [15] analysed compound textures, determining that well-structured configurations increased direct stiffness and damping, leading to higher critical speeds, with the optimal setup depending on texture distribution and depth. Matele et al. [16] compared textured and non-textured hydrodynamic JBs with circular, square, and densely packed square dimples, noting that partial texturing offers better stability than full texturing, with circular textures providing the most stability improvements. Sun et al. [17] used 3D computational fluid dynamics to study cavitation and journal whirl, concluding that cavitation increases whirl frequency and reduces stability. Yamada et al. [18] conducted a computational study of full square textures, showing reduced indirect stiffness factors and increased critical speeds, underscoring the significance of texture configuration for JB stability.

In addition to surface textures, nanoparticle-enhanced lubricants (nanolubricants) have been extensively researched for their potential to enhance JB dynamics. Abass et al. [19] proposed a framework to assess the effects of titanium dioxide (TiO_2) nanoparticles, revealing that these nanoparticles increase linear stiffness and damping coefficients. Suryawanshi et al. [20] experimentally confirmed that TiO_2 nanoparticle additives improve stiffness and damping across different lubricants. Hammza et al. [21] found that increasing nanoparticle concentrations boosts viscosity and pressure, though dynamic performance declines at excessive levels. Awad et al. [22] showed that larger TiO_2 content and particle size enhance stability limits and load capacity. Rahmani et al. [23] studied elliptical-bore JBs lubricated with dry microparticles under high temperatures, concluding that larger particles perform better than smaller ones,

especially at high eccentricity ratios. Byotra et al. [24,25] explored arc-shaped textures with aluminium oxide and copper oxide nanoparticles, finding that textures located in pressure-increasing regions significantly improve load capacity and reduce friction. Their follow-up work indicated that arc-shaped textures with an eccentricity ratio of 0.2 and a depth of 0.6 achieved the highest stiffness and damping, with nanoparticle additives particularly beneficial at elevated temperatures. Yin et al. [26] examined tribological properties in diesel engine cylinder liner-piston ring systems, discovering that combining surface textures with copper nanoparticles (CNPs) produced exceptional friction minimisation and wear durability due to the synergistic effects of texture storage capacity and CNP self-repair properties.

Extensive research has independently examined the effects of surface texturing and nanolubricants on JBs. However, their combined influence on the dynamic and thermal performance of JBs remains largely unexplored. This study bridges that gap by investigating the effects of rectangular surface texturing and TiO₂ nanoparticle additives on JB characteristics. Using computational fluid dynamics (CFD) in Fluent software, the analysis integrates elastic deformation through the fluid-structure interaction (FSI) approach and simulates cavitation using the Zwart–Gerber–Belamri method. The investigation evaluates performance across texture depths of 0.5, 1.0, 1.5, and 2.0, and eccentricity ratios (ϵ) ranging from 0.2 to 0.8, focusing on key regions such as convergence, divergence, and pressure-increasing zones. Following the identification of optimal texture depth and placement, the study examines the effects of TiO₂ nanoparticle concentrations (0.1% to 0.5% by weight) in the lubricant, assessing their impact on stiffness, damping, and thermal stability using the modified Krieger-Dougherty model.

2. THEORY

2.1 Governing equations

In this analysis, the Reynolds-averaged Navier–Stokes (RANS) equations were utilised to characterise the flow behaviour of the lubricant under the influence of surface motion. As noted

by [27], surface texturing on the bearing generates significant pressure gradients perpendicular to the textured surface. Consequently, solely relying on Reynolds's theory, which neglects inertia effects, may result in inaccuracies when predicting pressure distribution. The RANS and mass conservation equations are expressed as follows [28]:

$$\frac{\partial}{\partial x_i}(\rho u_i u_j) = -\frac{\partial p}{\partial x_i} + \frac{\partial}{\partial x_j} \left[\mu_l \left(\frac{\partial u_i}{\partial x_j} + \frac{\partial u_j}{\partial x_i} \right) \right] + \frac{\partial}{\partial x_j} (-\rho \overline{u_i' u_j'}) \quad (1)$$

$$\frac{\partial}{\partial x_i}(\rho u_i) = 0 \quad (2)$$

In equations (1) and (2), ρ represents the fluid density; u_i and u_j are the average velocity components in the x, y , and z directions; p denotes the hydrodynamic pressure; μ_f is the fluid viscosity; u_i' and u_j' represent velocity fluctuations; and $-\rho \overline{u_i' u_j'}$ is the Reynolds stress term. Here, $i, j = 1, 2, 3$ corresponds to the x, y , and z directions, respectively. In this study, Reynolds stress is modelled using the standard k - e models [28], where k denotes turbulent kinetic energy and e is the turbulent dissipation rate. The viscosity of the lubricating film is strongly affected by lubricant temperature; as the lubricant temperature rises, viscosity decreases, affecting the JB's performance. Therefore, heat transfer is incorporated in this study, necessitating an additional equation for energy conservation. The temperature distribution within the lubricant film is modelled through energy conservation, given by [28]:

$$\rho C_p V \cdot \nabla T = \nabla \cdot (\lambda \nabla T) - \tau \cdot \nabla V \quad (3)$$

Where C_p is the specific heat capacity of the liquid, $V \cdot \nabla T$ represents the convective heat transfer term due to the velocity field V within the lubricant, T denotes the film temperature, λ refers to thermal conductivity, τ is the shear stress, and ∇V denotes the lubricant's velocity gradients.

2.2 Cavitation modelling

In this investigation, cavitation phenomena were modelled utilising the mixture method available in CFD software, with effects analysed primarily through pressure variations. The model captures vapourisation within the lubricant film when the pressure drops below the vapourisation threshold, accurately depicting vapour-liquid two-phase flow, including simulating the

formation and growth of gas bubbles, a defining characteristic of cavitation. The Zwart–Gerber–Belamri multiphase cavitation approach was employed for this purpose [28,29], utilising the governing equation:

$$\frac{\partial}{\partial t}(\alpha_v \rho_v) + \nabla(\alpha_v \rho_v v) = R_g - R_c \quad (4)$$

Here, $\partial/\partial t(\alpha_v \rho_v)$ represents the time rate of change of vapour mass density, and $\nabla(\alpha_v \rho_v v)$ is the spatial transport of vapour mass due to the velocity field v . R_g and R_c denote the rate of mass transfer between the lubricants and vapour phases during cavitation. The final cavitation method assumes a uniform bubble size throughout the system [29]:

$$R_g = F_{vap} \frac{3\alpha_{nuc}(1-\alpha_v)\rho_v}{R_B} \sqrt{\frac{2(P_v-P)}{3\rho}} \quad \text{if } p \leq p_v \quad (5)$$

$$R_c = F_{cond} \frac{3\alpha_v \rho_v}{R_B} \sqrt{\frac{2(P-P_v)}{3\rho}} \quad \text{if } p > p_v \quad (6)$$

For these computations, the cavity radius R_B was set to 10^{-6} m, and the vaporisation pressure p_v was 29.185 kPa. The fractional nucleation volume α_{nuc} was assigned a value of 5×10^{-4} , with evaporation and condensation factors of $F_{vap} = 50$ and $F_{cond} = 0.01$, respectively [29].

2.3 Nanolubricants modelling

The use of nano-lubricants, particularly those containing TiO₂ nanoparticles, has emerged as a significant advancement in enhancing the performance of JBs. Compared to conventional engine oils, nano-lubricants provide superior viscosity, increased load capacity, and improved tribological properties [30]. In this study, TiO₂ nanoparticles were introduced into the base oil at varying concentrations, modifying key characteristics such as viscosity, density, specific heat capacity, and thermal conductivity, which are critical factors influencing bearing performance. These property changes were analysed using established mathematical models to better understand nano-lubricants' behaviour under operational conditions. The Krieger-Dougherty equation, widely used to model the viscosity of particle dispersions, was applied to describe the viscosity of the nano-lubricant μ_{nf} [31,32]:

$$\mu_{nf} = \mu_f \left(1 - \frac{\varphi}{\varphi_m}\right)^{-\eta \varphi_m} \quad (7)$$

Where φ is the nanoparticle volume fraction ranging from 0.001 to 0.005, φ_m is equal to 0.605, μ_f is the lubricant's viscosity, and η is equal to 2.5 [31-33]. The modified Krieger-Dougherty model introduced by Chen et al. [34] was utilised, incorporating the packing fraction of the aggregates to account for the aggregate structures formed by nanoparticles:

$$\mu_{nf} = \mu_f \left(1 - \frac{\varphi_a}{\varphi_m}\right)^{-2.5 \varphi_m} \quad (8)$$

The adjusted volume fraction (φ_a) is defined as:

$$\varphi_a = \varphi \left(\frac{a_a}{a}\right)^{3-D} \quad (9)$$

Here, a_a and a denote the radii of the aggregate and primary particles, respectively, and D is a fractional dimension, typically set to 1.8 for nanofluids [33]. By substituting $D = 1.8$ and $\varphi_m \cong 0.605$, the model simplifies as follows:

$$\mu_{nf} = \mu_f \left(1 - \frac{\varphi}{0.605} \left(\beta_{pack}\right)^{1.2}\right)^{-1.5125} \quad (10)$$

Where $\beta_{pack} = (a_a/a)$ represents the packing fraction, which varies with nanoparticle size and type. The volume fraction range selected for this study (0.001 to 0.005) aligns with findings by Binu et al. [35], who studied the shear viscosity of TiO₂ nanoparticles dispersed in lubricant at similar concentrations. Their dynamic light scattering analysis identified an average aggregate particle size of $a_a = 777$ nm, resulting in a packing fraction of $\beta_{pack} = 7.77$. This value was derived from peak measurements within a volume fraction range of 0.0001 to 0.005. These findings indicate that TiO₂ aggregates are approximately 7.77 times larger than primary particles. The experimental data strongly supports the applicability of the modified Krieger-Dougherty method to the selected volume fraction range, ensuring accurate predictions of viscosity behaviour. Temperature effects on viscosity were also considered. The temperature-dependent viscosity μ of the nano-lubricant was modelled using the exponential relationship [31]:

$$\mu = \mu_{nf} \exp(-\beta(T-T_i)) \quad (11)$$

Where β is the temperature sensitivity coefficient, T is the operating temperature, and T_i is the reference temperature. In addition to viscosity, the thermal conductivity of the nano-lubricant k_{nf} essential for heat transfer efficiency, was estimated using the Maxwell model [36]:

$$k_{nf} = k_f \frac{((k_n+2k_f)-2\varphi(k_f-k_n))}{((k_n+2k_f)+\varphi(k_f-k_n))} \quad (12)$$

Here, k_f represents the thermal conductivity of the lubricant and k_n denotes the thermal conductivity of TiO₂ nanoparticles [37]. The density of the nano-lubricant ρ_{nf} was calculated as [36]:

$$\rho_{nf} = (1-\varphi)\rho_f + \varphi\rho_n \quad (13)$$

Where ρ_f represents the lubricant's density and ρ_n denotes the density of TiO₂ nanoparticles. In addition, the specific heat capacity of the nano-lubricant $C_{p,nf}$ was determined as [38]:

$$\rho_{nf}C_{p,nf} = (1-\varphi)(\rho_fC_{pf}) + \varphi(\rho_nC_{pn}) \quad (14)$$

Where C_{pf} and C_{pn} represent the specific heat capacity of the lubricant and the TiO₂ nanoparticles, respectively. The physical properties of the TiO₂ nanoparticles used in these calculations, summarised in Table 1, were critical for accurately modelling these parameters.

Table 1. Nanoparticle properties [30].

Nanoparticles	TiO ₂
Particle size	30 nm
Purity	99.50%
C_p (J/kg. K)	690
K (W/m. K)	8.3
ρ (kg/m ³)	4230

2.4 Bearing performance

In analysing the performance of JBs, the reaction forces generated by the lubrication film surrounding the journal are crucial for understanding bearing dynamics, such as stability and load capacity. These forces, denoted as F_x and F_y along the x and y -axes, respectively, arise from pressure variations within the lubricant influenced by the journal's position. These forces are obtained by integrating the pressure distribution over the journal's surface, as detailed in [39], using the following expressions:

$$F_x = \int_0^{2\pi} \int_0^L p R \cos\theta d\theta dz \quad (15)$$

$$F_y = \int_0^{2\pi} \int_0^L p R \sin\theta d\theta dz \quad (16)$$

A perturbation method is applied to capture the dynamic behaviour of JBs, particularly their stiffness and damping effects. Small, controlled displacements and velocities are introduced to the journal using a user-defined function (UDF) within

the CFD simulation environment, allowing the observation of corresponding variations in reaction forces. The analysis begins with a steady-state solution, in which the journal is positioned at equilibrium, enabling the measurement of baseline pressure distribution and reaction forces. Once steady-state conditions are established, small displacements Δx and Δy are applied along the x and y -axes, resulting in corresponding force variations ΔF_x and ΔF_y . The resulting force variations are expressed through the following linearised equations, which incorporate both stiffness and damping effects [39]:

$$\Delta F_x = k_{xx} \Delta x + k_{xy} \Delta y + C_{xx} \dot{x} + C_{xy} \dot{y} \quad (17)$$

$$\Delta F_y = k_{yx} \Delta x + k_{yy} \Delta y + C_{yx} \dot{x} + C_{yy} \dot{y} \quad (18)$$

In these equations, Δx and Δy represent the journal's displacements from its equilibrium position along the x - and y -axes, while \dot{x} and \dot{y} denote the velocity components of the journal along the x - and y -axes. The stiffness factors K_{xx} , K_{xy} , K_{yx} , and K_{yy} quantify the forces' sensitivity to displacements. In contrast, the damping factors C_{xx} , C_{xy} , C_{yx} , and C_{yy} characterise the forces' sensitivity to the journal's velocities. The stiffness components determine the system's response when the journal is stationary (i.e., $\dot{x} = 0$ and $\dot{y} = 0$). Under these conditions, the stiffness coefficients can be determined by analysing the force variations induced by the applied displacements Δx and Δy , as follows [39]:

$$k_{xx} = \frac{\Delta F_{xx}}{\Delta x}, k_{yx} = \frac{\Delta F_{yx}}{\Delta x}, k_{xy} = \frac{\Delta F_{xy}}{\Delta y}, k_{yy} = \frac{\Delta F_{yy}}{\Delta y} \quad (19)$$

In the subsequent phase, damping effects are isolated by applying small velocity perturbations along the x - and y -axes while keeping the displacements constant. The resulting force variations induced by these velocity perturbations enable the determination of the damping coefficients as follows [39]:

$$C_{xx} = \frac{\Delta F_{xx}}{\Delta \dot{x}}, C_{yx} = \frac{\Delta F_{yx}}{\Delta \dot{x}}, C_{xy} = \frac{\Delta F_{xy}}{\Delta \dot{y}}, C_{yy} = \frac{\Delta F_{yy}}{\Delta \dot{y}} \quad (20)$$

Both stiffness and damping factors are expressed in dimensionless form to enable comparison and generalisation across various operating conditions and bearing geometries. The normalisation of stiffness factors uses a characteristic stiffness scale, $k_0 = \mu R \omega / c$. This normalisation defines the dimensionless stiffness coefficients \bar{k}_{xx} , \bar{k}_{yx} , \bar{k}_{xy} , and \bar{k}_{yy} as follows [40]:

$$\bar{k}_{xx} = \frac{k_{xx}}{k_0}, \bar{k}_{yx} = \frac{k_{yx}}{k_0}, \bar{k}_{xy} = \frac{k_{xy}}{k_0}, \bar{k}_{yy} = \frac{k_{yy}}{k_0} \quad (21)$$

Similarly, the damping coefficients are normalised using a characteristic damping scale, $C_0 = \mu R/c$. The dimensionless damping coefficients, \bar{C}_{xx} , \bar{C}_{yx} , \bar{C}_{xy} , and \bar{C}_{yy} , are subsequently defined as follows [40]:

$$\bar{C}_{xx} = \frac{C_{xx}}{C_0}, \bar{C}_{yx} = \frac{C_{yx}}{C_0}, \bar{C}_{xy} = \frac{C_{xy}}{C_0}, \bar{C}_{yy} = \frac{C_{yy}}{C_0} \quad (22)$$

3. COMPUTATIONAL ANALYSIS

3.1 Geometric Model

Figure 1a presents a schematic of a partially textured JB in Cartesian coordinates, with the relevant dimensions detailed in Table 2. In this schematic, points O_B and O_J represent the centres of the bearing and the shaft, respectively, where the variable e denotes the eccentricity. This study adopts a simplified model, assuming the journal remains aligned with the bearing. The bearing surface is divided into three main zones: the convergence zone, the divergence zone, and the pressure-increase zone, as depicted in Figure 1b. Each zone contains six textures in the axial direction and eight in the circumferential direction, strategically designed to optimise lubricant flow.

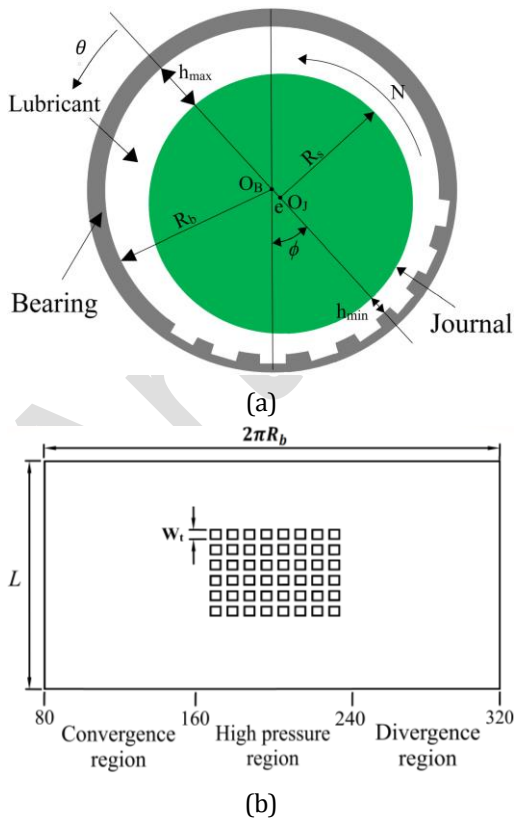


Fig. 1. Illustration of the textured JB: (a) the coordinate system; (b) the detailed view of the textured JB surface [41].

Rectangular textures are used in the simulation due to their simplicity in manufacturing and predictable flow patterns. Each texture is characterised by its depth and width (W_t), with W_t uniformly set to 1 mm. The midpoint spacing between adjacent textures is maintained at 1.5 mm, ensuring even distribution across the bearing surface. Texture depths (D_t) range from 0.5 to 2.0 relative to the minimum lubricant thickness, facilitating an analysis of how pronounced surface features influence lubricant behaviour and pressure distribution. Although the Reynolds equation is commonly used in bearing analysis, it is limited in accurately predicting pressure distributions when surface textures are pronounced, as it may underestimate pressure gradients due to the neglect of inertial effects. The Reynolds-Averaged Navier-Stokes (RANS) equations are utilised to overcome these limitations, providing a more robust framework for capturing the complex flow dynamics induced by pronounced surface textures.

Table 2. Geometrical parameters for the investigated JB.

Symbol	Parameters	Values
R_{bi}	Bearing radius	15 mm
R_{bo}	Bearing Outside diameter	17 mm
L	Bearing Length	20 mm
c	Radial clearance	30 μ m
ε	Eccentricity ratios	0.2-0.8
ϕ	Attitude angle	45 °
N	Rotating speed	1000 rpm

3.2 Meshing

The bearing and lubricant domains were discretised using SOLID186 elements, employing sweep, edge scaling, and face meshing techniques to achieve an efficient and accurate mesh. The bearing was meshed with $400 \times 20 \times 40$ elements along the circumferential, radial, and width axes. The lubricating film was discretised with $400 \times 10 \times 40$ elements. This meshing arrangement was determined through a grid sensitivity analysis, which revealed that further refinement caused minimal changes in critical performance metrics, such as lubricant pressure, with variations remaining below 0.5%, as documented in Table 3. This configuration was deemed optimal, offering a balanced trade-off between accuracy and computational efficiency, and was thus adopted for all subsequent simulations. Figures 2a and 2b illustrate the meshed lubricant film and bearing, respectively, with markers

indicating key regions: Marker 1 represents the inlet, Marker 2 the outlet, Markers 3 and 4 denote the internal and external surfaces of the lubricant film, and Markers 5 and 6 correspond to the internal and external surfaces of the bearing. In the model, the journal is treated as a rigid body. The external surface of the bearing is defined as a fixed support, while its internal surface serves as a fluid-solid interface. Similarly, the external surface of the lubricant film acts as an interface, and its internal surface is designated as a rotating wall.

Table 3. Grid sensitivity analysis of the lubricating film.

Elements (Circumferential × Thickness × Axial)	Pressure (kPa)
200×5×20	354.307
300×5×30	350.921
400×5×40	349.367
400×6×40	348.471
400×7×40	348.059
400×8×40	347.944
400×9×40	347.814
400×10×40	347.809
400×11×40	347.804
400×12×40	347.803

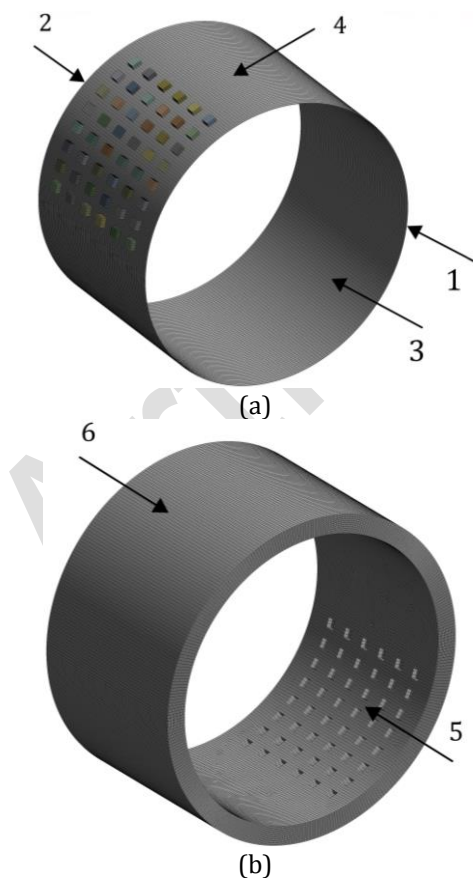


Fig. 2. Mesh configurations for lubricant and bearing with boundary conditions: (a) lubricant mesh; (b) bearing mesh.

3.3 Fluid structure interaction (FSI)

The FSI approach models the intricate mutual effects between lubricant flow and bearing deformation. Within the ANSYS software suite, ANSYS Fluent simulates the dynamic behaviour of the lubricant, while ANSYS Mechanical models the mechanical response of the bearing structure. This two-way FSI methodology operates iteratively, enabling the lubricant and bearing models to continuously adjust to each other's evolving conditions. Specifically, ANSYS Mechanical calculates the deformations of the bearing, which ANSYS Fluent incorporates to refine the lubricant's hydrodynamic pressure and force distributions. This tightly coupled process provides a highly accurate and dynamic representation of the interactions between the lubricant flow and the bearing structure, thereby significantly improving the precision of the simulation results. The detailed material properties and parameters of the lubricant and bearing domains are summarised in Table 4, providing essential input data for the FSI simulations.

Table 4. Physical characteristics of the lubricant and bearing domain.

Parameters	Values
Fluid density	822 kg.m ⁻³
Vapour density	1.29 kg.m ⁻³
Fluid viscosity	0.037 Pa.s
vapour viscosity	5.953 × 10 ⁻⁶ Pa.s
bearing density	8.935 g.cm ⁻³
Young modulus	128 GPa
Poisson ratio	0.34

3.4 Assumptions and boundary conditions

In the lubricant domain, inlet and outlet boundary conditions are defined to simulate thermal and fluid flow behaviour accurately. The lubricant enters the bearing clearance at a constant temperature of 40°C, representing typical operating conditions, with the pressure maintained at 1 bar. The edges of the lubricant film are defined as a pressure inlet and a pressure outlet, each assigned a gauge pressure of zero. The heat generated by viscous dissipation within the lubricant film affects the outlet temperature, offering a detailed thermal profile of the lubricant flow. The inner surface of the lubricant domain is modelled as a moving wall to simulate journal rotation, while the outer surface remains stationary. The shaft axis position is specified by defining the x, y, and z coordinates to establish the

origin of the rotation axis. Both the bearing and journal surfaces are assumed to be adiabatic, indicating that no heat transfer occurs through these surfaces. This adiabatic condition isolates the internal heat dynamics of the lubricant, enabling the analysis to focus exclusively on heat generation and retention within the lubricant film, free from interference by heat exchange with solid surfaces. The lubricant is assumed to be incompressible, with its viscosity modelled as a temperature-dependent property. A dynamic mesh method incorporating a smoothing technique is employed to adapt to variations in lubricant film thickness during operation. The RANS and energy equations are solved under steady-state conditions to capture the flow and thermal dynamics. A pressure-based solver and the SIMPLE pressure-velocity coupling approach ensure simulation accuracy and efficiency. To ensure numerical precision, the second-order upwind method is utilised to discretise the momentum equations, while the QUICK scheme is applied for volume fraction calculations. Convergence criteria are defined by a residual threshold of 10^{-6} , ensuring high accuracy and stability in the simulation results.

3.5 Solution setup

The lubricant film and bearing models were developed and meshed using Ansys 2021 software, incorporating varying eccentricity, texture depth, and texture position, as illustrated in Figure 3.

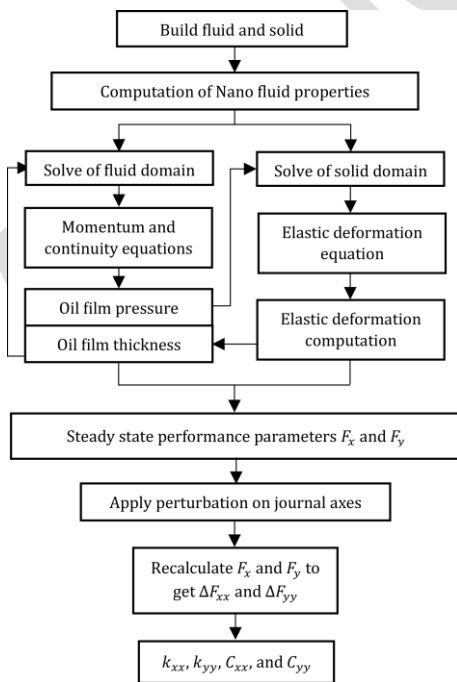


Fig. 3. Flowchart for calculation of stiffness and damping coefficients.

Reaction forces were computed using equations (15) and (16) by evaluating the equilibrium pressure profile through the FSI method described in Section 3.3. Subsequently, perturbations (Δx , Δy , \dot{x} , and \dot{y}) were introduced to the journal surface through a UDF. The displacements and velocities of the journal along the x - and y -axes resulted in force variations (ΔF_{xx} and ΔF_{yy}). These force variations were subsequently utilised to compute the stiffness and damping factors, following the procedure outlined in equations (19) and (20). The entire process for computing the stiffness and damping factors is summarised in the flowchart provided in Figure 3.

3.6 Validation

The computational model was validated using experimental data from Yamada et al. [18], with stiffness factors (K_{xx} and K_{yy}) and damping factors (C_{xx} and C_{yy}) plotted against the Sommerfeld number. Figure 4 illustrates this comparison, demonstrating strong agreement between the computational and experimental results. The Sommerfeld number (S), a dimensionless parameter representing bearing operating conditions, was calculated using the following equation:

$$S = \frac{W}{\mu N \psi L D} \quad (23)$$

Where W is the load-bearing capacity, and $\psi = C/R$ is the clearance ratio. The validation results showed that the computational model accurately predicts the variation of stiffness and damping factors with the Sommerfeld number. The trends observed computationally for stiffness factors (K_{xx} and K_{yy}), including reductions for textured bearings, matched well with experimental findings. Similarly, damping factors (C_{xx} and C_{yy}) exhibited consistent trends, underscoring the impact of surface texturing. Minor discrepancies were attributed to the perturbation methods employed in this study, as opposed to the sinusoidal excitation used in experimental settings. These differences highlight the sensitivity of JB dynamics to variations in force application without compromising the model's accuracy. Thus, the validated model is reliable for investigating the complex dynamics of journal bearings, including textured designs. The key parameters required to replicate these results are summarised in Table 5.

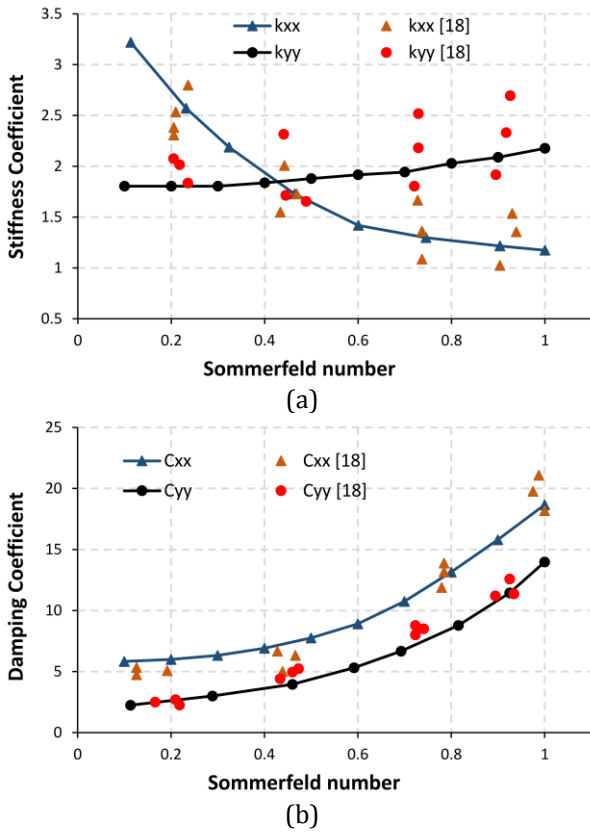


Fig. 4. Comparison of stiffness and damping factors between present work and literature [18].

Table 5. Essential Parameters for Validation [18].

Parameter	Value
D	50.05 mm
L	50 mm
C	31 μm
Dimple depth (ht)	25 μm
Dt	1.0
W	Adjusted to Sommerfeld number
μ	0.002 Pa
ρ	850 kg/m^3
S	0.1-1

4. RESULTS AND DISCUSSION

The dynamic and thermal characteristics of textured JBs are evaluated across a range of Dt and ε . These evaluations are conducted within the convergence, divergence, and pressure-increase zones of the bearing. Comparative analyses of these zones are performed to identify parameter values that optimise performance, including enhanced dynamic stability and improved thermal behaviour. Additionally, TiO_2 nanoparticles are incorporated into the base lubricant within these regions to assess their potential for improving bearing performance. The key outcomes of this examination are outlined below:

4.1 Effect of cavitation and elastic deformation

Figure 5 illustrates the pressure profiles for scenarios with and without the consideration of cavitation effects. A comparison reveals that the maximum pressure in the JB without cavitation is higher than that with cavitation, confirming that cavitation reduces the peak positive pressure accumulation.

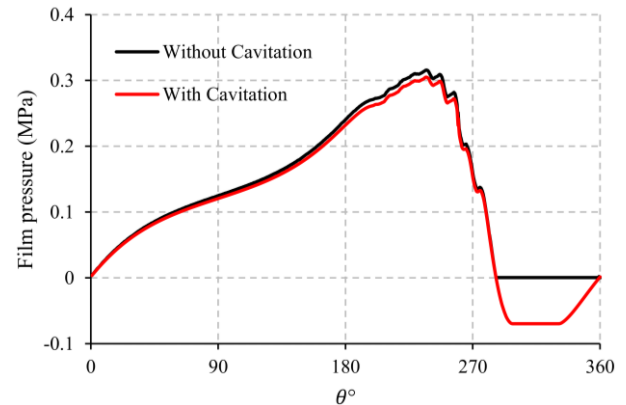


Fig. 5. Pressure profile of JB with and without cavitation.

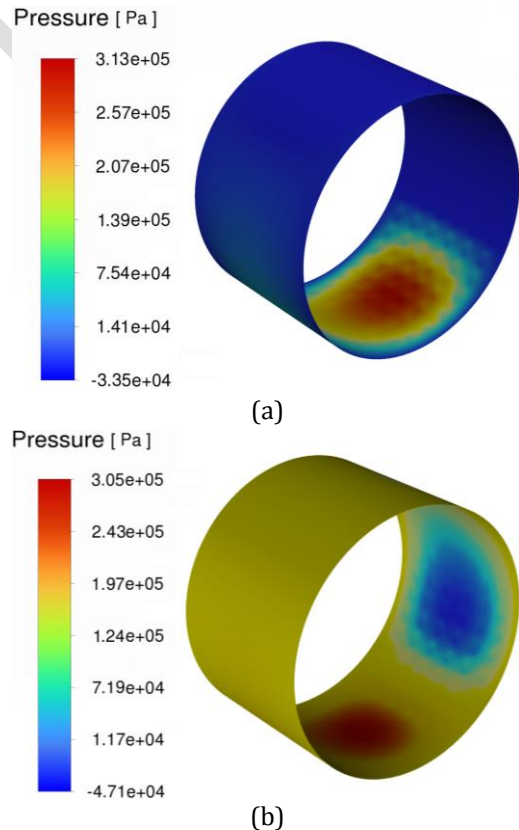


Fig. 6. Pressure contours generated for JB.

The pressure contours in Figure 6 further emphasise the cavitation zones, visually demonstrating how cavitation disrupts the lubricant's pressure distribution. Figure 6a

highlights regions of pressure accumulation and pressure drop, while Figure 6b shows how cavitation alters the distribution, reducing pressure build-up and eliminating the pressure drop.

Figure 7 compares pressure profiles with and without considering FSI. The results indicate a decrease in peak pressure when elastic deformations are accounted for, compared to the maximum pressure in the rigid case. Figure 8 illustrates the elastic deformation of the bearing, which enlarges the gap between the shaft and the bearing. This increased gap accommodates more lubricant, thereby lowering the maximum pressure generated compared to the rigid assumption.

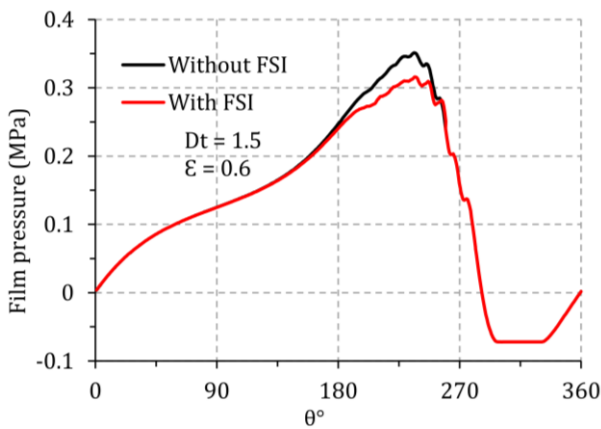


Fig. 7. Pressure profile of JB with and without FSI.

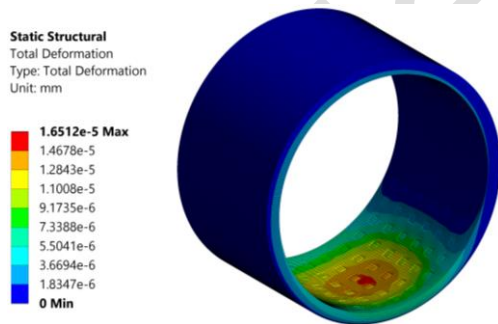
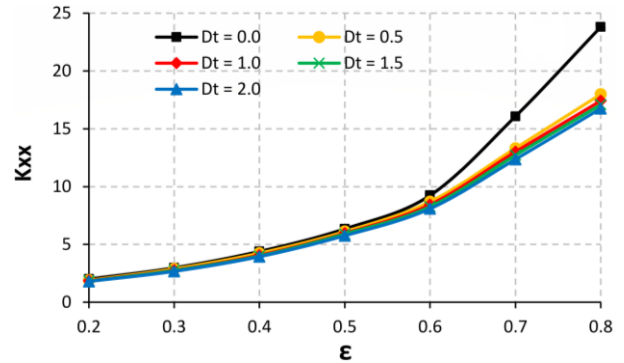


Fig. 8. Deformation contour of JB at ϵ of 0.6 and Dt of 1.5.

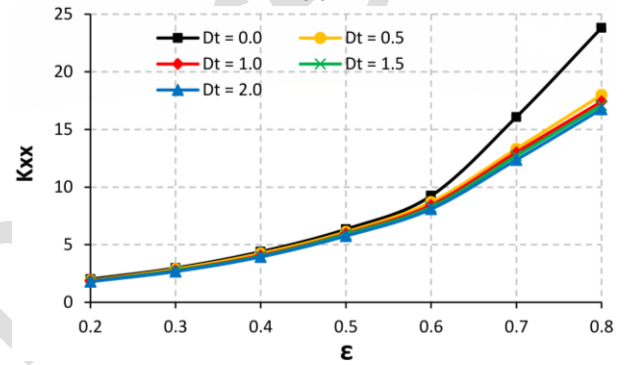
4.2 Effect of texture depths on convergence region

The results highlight the significant influence of Dt on stiffness (K_{xx} and K_{yy}), damping (C_{xx} and C_{yy}), and temperature within the convergence region of the JB, as shown in Figures 9 and 10. Stiffness factors decrease consistently with increasing Dt due to disruptions in pressure build-up and lubricant flow stability. For example, K_{xx} at $\epsilon = 0.7$ decreases from 16.07 at $Dt = 0.0$ to 12.36 at $Dt = 2.0$, while K_{yy} at the same ϵ

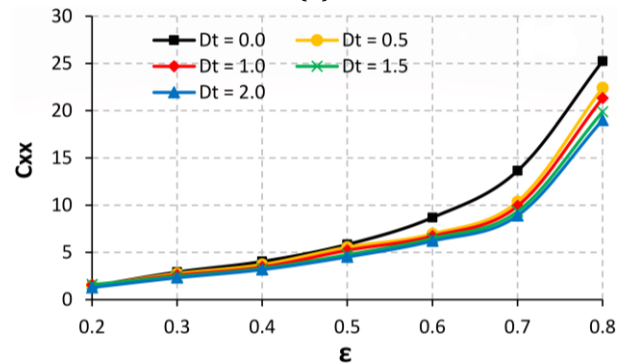
decreases from 31.68 at $Dt = 0.0$ to 26.61 at $Dt = 2.0$. Moderate depths ($Dt = 0.5$ to 1.0) provide slight stabilisation, with smaller reductions observed; for instance, K_{xx} at $\epsilon = 0.5$ decreases from 6.34 at $Dt = 0.0$ to 5.96 at $Dt = 1.0$.



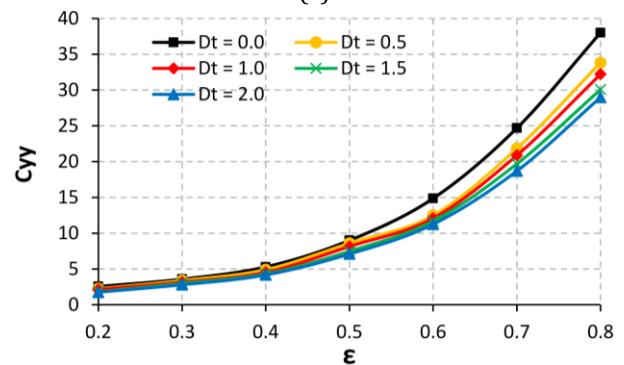
(a)



(b)



(c)



(d)

Fig. 9. Stiffness and damping factors K_{xx} , K_{yy} , C_{xx} , and C_{yy} against the Dt and ϵ in the convergence region.

These trends are consistent with findings by Li et al. [42] and Khatri et al. [43], which associate textures in the convergence region with reduced hydrodynamic lift due to disrupted pressure gradients. The close similarity in stiffness factor values at lower ϵ can be attributed to the dominant hydrodynamic effects stabilising the lubricant flow at moderate displacements, where texture influence is less pronounced. However, as ϵ increases, the effect of Dt on stiffness factors becomes more apparent due to amplified pressure gradients and the reduced film thickness, leading to larger divergences in stiffness values. Damping factors also decline with increasing Dt , particularly beyond $Dt = 1.5$, due to turbulence and flow separations. For example, C_{xx} at $\epsilon = 0.8$ decreases from 25.22 at $Dt = 0.0$ to 19.0 at $Dt = 2.0$, while C_{yy} at the same ϵ reduces from 38.0 at $Dt = 0.0$ to 28.98 at $Dt = 2.0$. These reductions align with studies by Byotra et al. [25] and Meng et al. [15], which attribute decreased damping in the convergence region to fluid instability caused by excessive texture depths. Temperature trends indicate initial reductions at moderate depths ($Dt = 0.5$ to 1.5) due to enhanced convective heat transfer, as shown in Figure 10. For instance, at $\epsilon = 0.5$, temperature decreases from 49.55°C at $Dt = 0.0$ to 46.75°C at $Dt = 1.5$. However, deeper textures ($Dt > 1.5$) result in localised overheating, as observed at $\epsilon = 0.8$, where temperature increases slightly from 65.75°C at $Dt = 1.5$ to 66.54°C at $Dt = 2.0$.

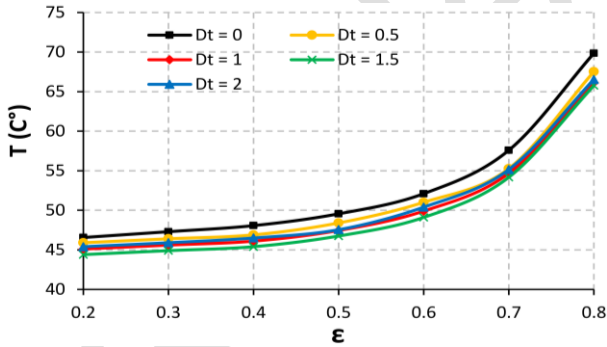


Fig. 10. Temperature against the Dt and ϵ .

These results are consistent with findings by Kango et al. [44], who identified stagnation zones and increased shear heating as primary causes of thermal inefficiencies. In conclusion, textures in the convergence region reduce stiffness and damping while providing limited thermal benefits at moderate depths. Excessive depths exacerbate performance degradation due to increased instability and thermal inefficiencies. These findings underscore the challenges of texturing in the convergence region, aligning closely with existing literature.

4.3 Effect of texture depths on pressure increasing region

The pressure-increasing region shows enhanced stiffness, damping, and temperature at moderate Dt compared with the convergence region. Figures 11 and 12 illustrate how these parameters respond to variations in Dt and ϵ .

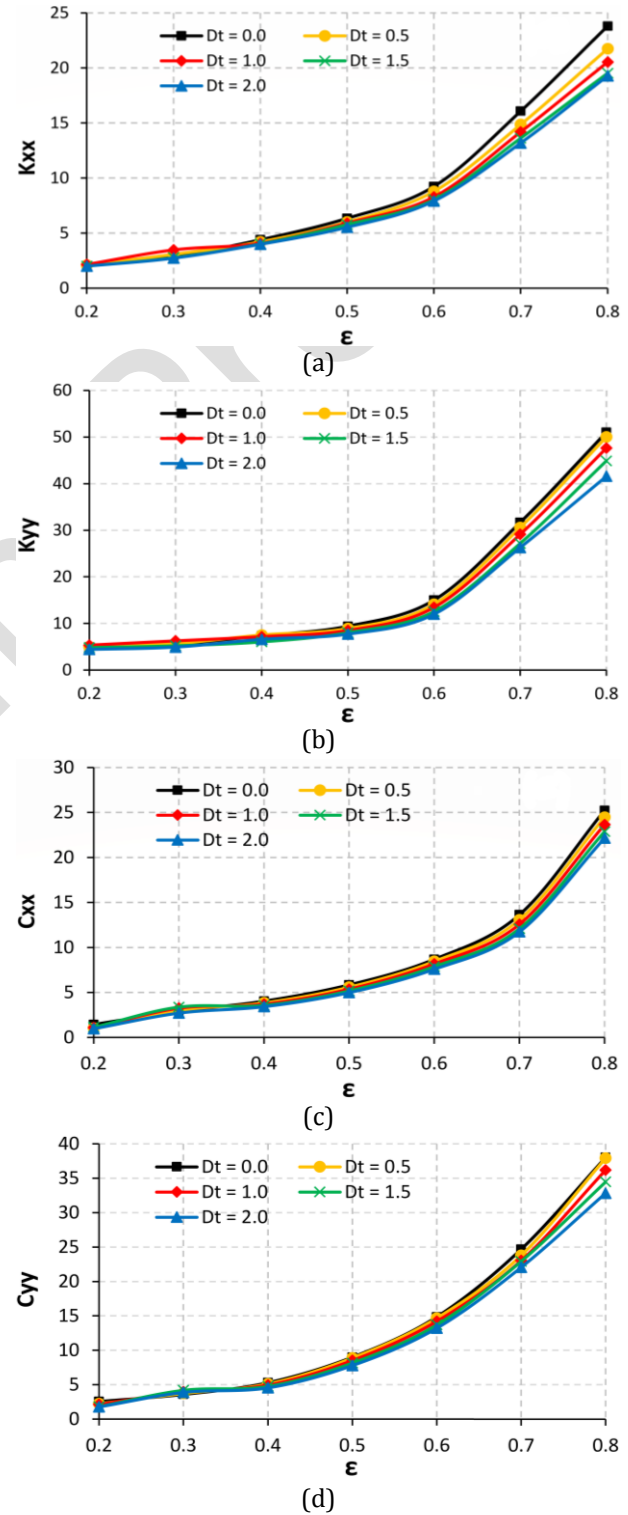


Fig. 11. K_{xx} , K_{yy} , C_{xx} , and C_{yy} against the Dt and ϵ in the pressure-increasing zone.

Moderate texture depths ($Dt = 0.5$ to 1.0) enhance stiffness through the wedge effect, where localised pressure gradients stabilise the lubricant film and increase its load capacity. This enhancement, shown in Figures 11a and 11b, is most effective at eccentricities ($\varepsilon = 0.2$ to 0.4), where stiffness peaks due to optimal flow dynamics. Byotra et al. [25] corroborate this behaviour, reporting significant improvements in stiffness for similar textures applied in the pressure-increasing region. However, at greater depths ($Dt > 1.5$), Figures 11a and 11b show a decline in stiffness due to flow disruptions and localised pressure losses. This behaviour aligns with findings by Li et al. [42], who noted reduced hydrodynamic lift and stability at excessive texture depths due to cavitation and turbulence.

Damping coefficients (C_{xx} and C_{yy}), as visualised in Figures 11c and 11d, exhibit similar trends. Moderate textures improve damping by stabilising fluid flow and dissipating energy through controlled turbulence. This improvement is particularly evident at eccentricities ($\varepsilon = 0.2$ to 0.4), where damping coefficients reach their maxima. Byotra et al. [25] reported an enhancement in damping under comparable conditions. However, deeper textures ($Dt > 1.5$) reduce damping efficiency, as shown in Figures 11c and 11d, due to chaotic turbulence and cavitation. These effects are further exacerbated by flow separation zones, which destabilise the fluid film, consistent with observations by Li et al. [42]. Figure 12 highlights the role of Dt in temperature control. Moderate textures ($Dt = 0.5$ to 1.0) reduce lubricant temperatures by facilitating convective heat transfer and enhancing mixing. These depths prevent thermal stratification and maintain lower operating temperatures.

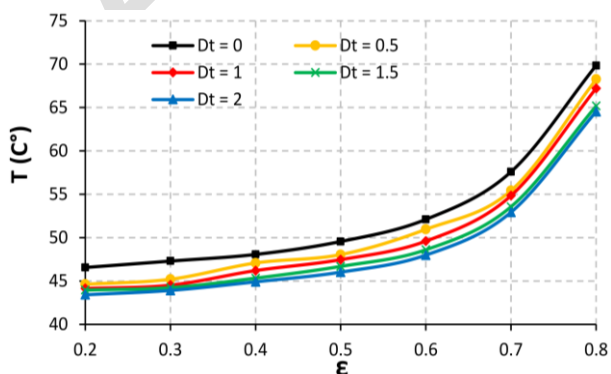


Fig. 12. Temperature against the Dt and ε .

Kango et al. [44] observed a reduction in average lubricant temperature with optimally designed surface textures. Conversely, deeper textures ($Dt > 1.5$) result in flow stagnation zones that impede heat dissipation, leading to localised overheating. This effect becomes even more pronounced at higher eccentricities ($\varepsilon > 0.6$), where thinner lubricant films intensify shear-induced heating. In conclusion, Figures 11 and 12 demonstrate that moderate texture depths ($Dt = 0.5$ to 1.0) achieve the optimal balance of stiffness, damping, and temperature control. These textures enhance hydrodynamic performance by improving load-carrying capacity, stabilising energy dissipation, and reducing lubricant temperatures. Beyond this range, deeper textures compromise performance through disruptions in flow stability and heat dissipation, particularly at high eccentricities. These results align with studies by Byotra et al. [25], Li et al. [42], and Kango et al. [44], reinforcing the necessity of geometric and operational optimisation in JB design.

4.4 Effect of texture depths on divergence region

A decline in stiffness and damping factors, coupled with a temperature rise, is observed in the divergence region as Dt increases, compared with the more stable performance of the convergence and pressure-increasing zones, as shown in Figures 13 and 14. The divergence region experiences performance challenges, primarily due to flow separations and cavitation, which disrupt pressure recovery and energy dissipation. Figures 13a and 13b show that stiffness factors decline consistently with increasing Dt across all ε . For instance, K_{xx} at $\varepsilon = 0.7$ decreases from 16.07 at $Dt = 0.0$ to 10.64 at $Dt = 2.0$, while K_{yy} at the same ε reduces from 31.68 at $Dt = 0.0$ to 25.07 at $Dt = 2.0$. These reductions are even more pronounced at higher ε , where the lubricant film becomes thinner, exacerbating flow instability. The decline is less severe at moderate depths ($Dt = 0.5$ to 1.0), as seen at $\varepsilon = 0.5$, where K_{xx} reduces from 6.34 at $Dt = 0.0$ to 5.21 at $Dt = 1.0$. These trends suggest that texturing in the divergence region weakens pressure recovery and reduces hydrodynamic lift.

Damping factors follow a similar downward trend with increasing Dt , reflecting the loss of fluid stability and energy dissipation capacity in the divergence region. For example, C_{xx} at $\varepsilon = 0.8$ decreases from 25.22 at $Dt = 0.0$ to 17.68 at $Dt = 2.0$, while C_{yy} at the same ε reduces from 38.0 at $Dt = 0.0$ to 25.31 at $Dt = 2.0$. Moderate depths provide slightly better performance, as seen at $\varepsilon = 0.6$, where C_{xx} decreases from 8.68 at $Dt = 0.0$ to 5.68 at

$Dt = 1.0$. However, deeper textures ($Dt > 1.5$) exacerbate chaotic turbulence and flow separations, reducing damping efficiency significantly. These trends highlight the challenges of maintaining fluid stability in the divergence region, particularly with excessive texture depths.

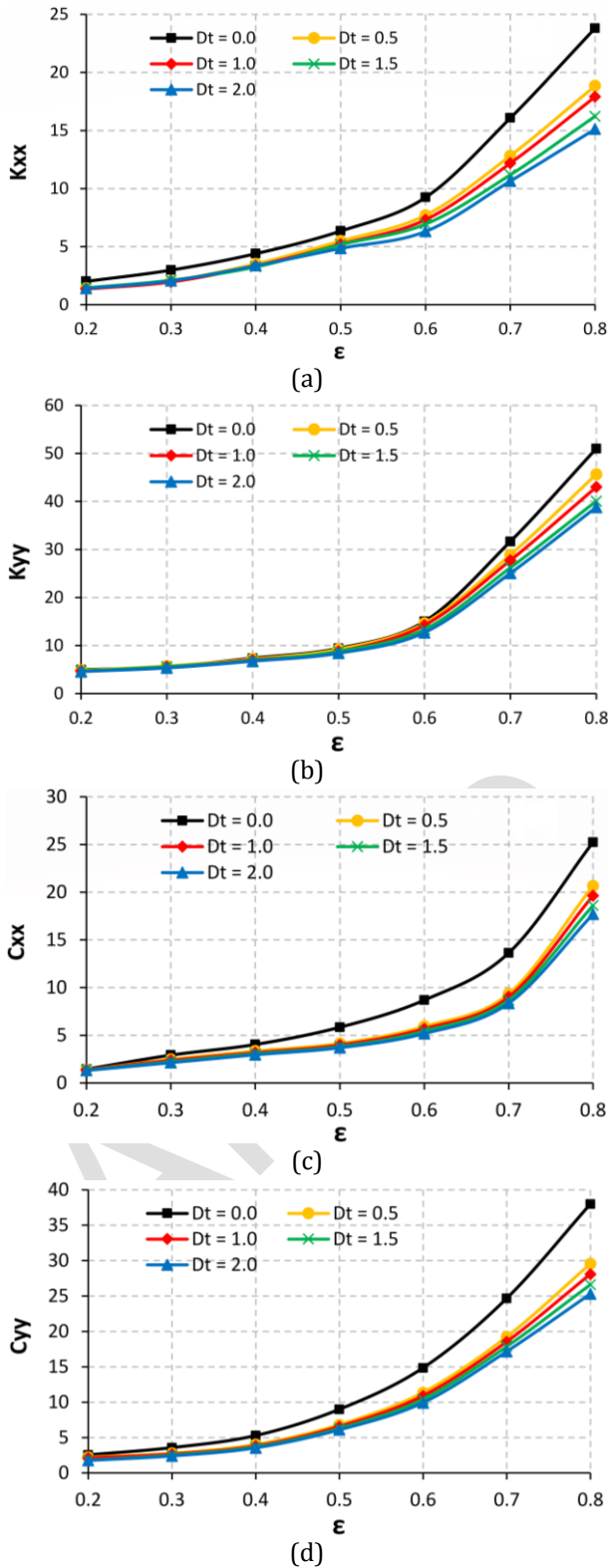


Fig. 13. Stiffness and damping factors K_{xx} , K_{yy} , C_{xx} , and C_{yy} against the Dt and ϵ in the divergence zone.

Figure 14 shows that temperature trends in the divergence region differ from stiffness and damping. Moderate depths ($Dt = 0.5$ to 1.0) reduce temperature due to improved convective heat transfer and mixing. For example, at $\epsilon = 0.5$, temperature decreases from 49.55°C at $Dt = 0.0$ to 47.9°C at $Dt = 1.0$. However, at greater depths ($Dt > 1.5$), temperatures rise due to flow stagnation and increased shear-induced heating, as evident at $\epsilon = 0.8$, where temperature increases from 66.2°C at $Dt = 1.0$ to 69.9°C at $Dt = 2.0$. These findings suggest that while moderate textures provide thermal benefits, deeper textures introduce inefficiencies. In conclusion, stiffness and damping in this region decline with increasing texture depth due to disrupted flow stability and reduced hydrodynamic performance. Moderate depths ($Dt = 0.5$ to 1.0) offer slight improvements in thermal management, but excessive depths ($Dt > 1.5$) exacerbate performance degradation, particularly for damping and stiffness. The observed trends emphasise the need for careful optimisation of texture parameters to mitigate flow separations and cavitation effects in this region.

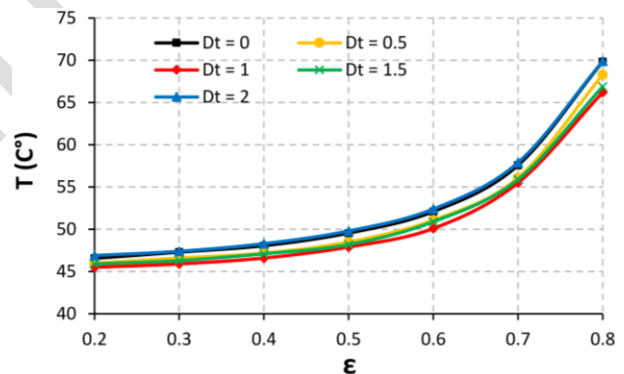


Fig. 14. Temperature against the Dt and ϵ .

4.5 Effect of TiO_2 additives

The integration of TiO_2 nanoparticles and surface texturing enhances the thermal performance of JBs. As shown in Figure 15, lubricant film temperatures consistently decrease with increasing Dt and w_t . At $Dt = 0.0$, the temperature starts at 47.30°C without nanoparticles, gradually decreasing to 44.8°C as the w_t increases. At $Dt = 2.0$, temperatures further drop to a range of 43.92°C to 41.42°C , demonstrating the combined effectiveness of Dt and TiO_2 nanoparticles in improving heat dissipation. Yasir et al. [30] reported that TiO_2 nanoparticles reduce oil film temperatures under high thermal loads by stabilising the lubricant film and

enhancing heat transfer. These nanoparticles efficiently conduct heat within the lubricant, while surface texturing creates micro-reservoirs that uniformly distribute the enhanced lubricant.

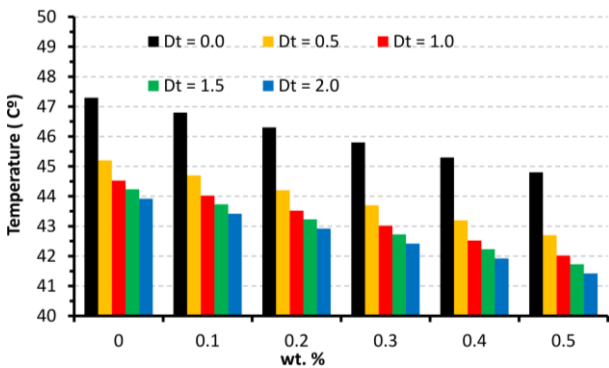


Fig. 15. Variations in temperature against the Dt and Wt. of TiO₂ nanoparticles at $\epsilon = 0.3$ in the pressure-increasing region.

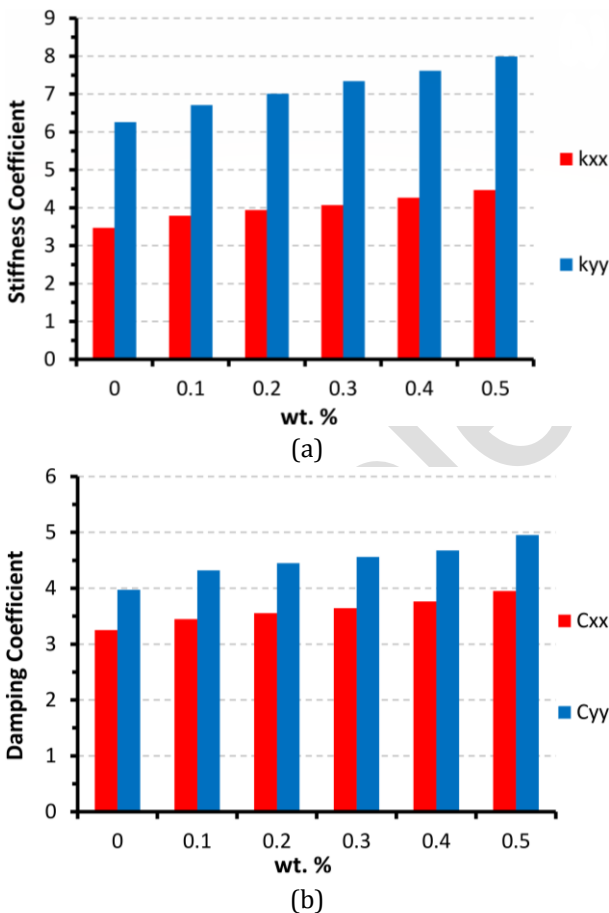


Fig. 16. Variations in stiffness and damping factors against the Wt. of TiO₂ nanoparticles at eccentricity = 0.3 and Dt = 1.0 in the pressure-increasing region.

Kango et al. [44] observed that texturing alone reduces lubricant temperatures, and the superior thermal properties of TiO₂ nanoparticles amplify this effect. Together, Dt and wt improve heat

dissipation, reduce hotspots, and enhance operational efficiency. TiO₂ nanoparticles also significantly improve stiffness (K_{xx} and K_{yy}) and damping (C_{xx} and C_{yy}) factors, as illustrated in Figure 16. Stiffness increases consistently with rising wt, from 3.47 and 6.26 at wt = 0.0 to 4.47 and 7.99 at wt = 0.5, respectively, while damping improves from 3.25 and 3.97 at wt = 0.0 to 3.95 and 4.98 at wt = 0.5. Byotra et al. [45] attributed these enhancements to the improved viscosity and stability of the hydrodynamic film. Additionally, TiO₂ nanoparticles reduce wear and friction at mating surfaces by forming protective films, as highlighted by Ilie et al. [46]. This reduction minimises surface roughness, prevents material degradation, and ensures consistent alignment of the journal and bearing surfaces. By mitigating heat generation from frictional losses, these nanoparticles help maintain lower temperatures, stabilising lubricant viscosity and stiffness factors. Smoother surface interactions further enhance energy dissipation and damping capacity by reducing fluid instabilities and cavitation [47]. These combined effects support consistent pressure gradients and improved overall system stability, underscoring the significant role of TiO₂ nanoparticles in optimising bearing performance.

5. CONCLUSION

In this study, the impact of rectangular textures with depths varying between 0.5 and 2.0 on the inner bearing surface was rigorously examined across convergence, divergence, and pressure-rise regions to assess their influence on the dynamic and thermal characteristics of the JB. Furthermore, the study evaluated the enhancement of bearing performance by introducing TiO₂ nanoparticles into the lubricant, with concentrations ranging from 0.1% to 0.5% by weight. The conclusions presented below are derived directly from the data and analysis conducted in this research:

- Surface texture in the pressure-increasing region showed the most significant improvements in stiffness (K_{xx} and K_{yy}) and damping (C_{xx} and C_{yy}) factors. Moderate texture depths (Dt = 0.5 to Dt = 1.0) increased stiffness by 17.5% and 11.8% and damping by 18.5% and 19.3%, respectively, compared to a smooth surface. In contrast, excessive texture depths (Dt > 1.5) in other regions caused declines in stiffness and damping factors.

- TiO₂ nanoparticles and moderate texture depths synergistically reduced lubricant temperatures. At Dt = 2.0 and wt = 0.5 %, temperatures in the pressure-increasing region dropped to 41.42°C compared to 47.30°C for a smooth surface without nanoparticles.

This study introduces a practical CFD approach for analysing the stiffness and damping factors of textured JB with TiO₂ additives, offering a valuable tool for minimising experimental efforts and aiding bearing designers. While offering valuable insights, this study is limited by the focus on lubricant film temperatures, with no analysis of heat generation or thermal deformation in solid components. Dynamic characteristics were examined, but further research is recommended under varying speed and load conditions. Future studies should also explore other nanoparticle types or hybrid lubrication systems. Expanding the CFD framework to include thermo-elastic-hydrodynamic simulations would enhance the applicability of these findings for bearing design.

REFERENCES

- [1] T. V. V. L. N. Rao and J. T. Sawicki, "Dynamic coefficient prediction in multi-lobe journal bearings using a mass conservation algorithm," *Tribology Transactions*, vol. 46, no. 3, pp. 414–420, Jan. 2003, doi: [10.1080/10402000308982645](https://doi.org/10.1080/10402000308982645).
- [2] S. Hamdavi, H. H. Ya, and T. V. V. L. N. Rao, "Effect of surface texturing on hydrodynamic performance of journal bearings," *ARPN Journal of Engineering and Applied Sciences*, vol. 11, no. 1, pp. 172–176, Jan. 2016.
- [3] N. Tala-Ighil, M. Fillon, and P. Maspeyrot, "Effect of textured area on the performances of a hydrodynamic journal bearing," *Tribology International*, vol. 44, no. 3, pp. 211–219, Oct. 2010, doi: [10.1016/j.triboint.2010.10.003](https://doi.org/10.1016/j.triboint.2010.10.003).
- [4] S. Kango, D. Singh, and R. K. Sharma, "Numerical investigation on the influence of surface texture on the performance of hydrodynamic journal bearing," *Meccanica*, vol. 47, no. 2, pp. 469–482, Jul. 2011, doi: [10.1007/s11012-011-9460-y](https://doi.org/10.1007/s11012-011-9460-y).
- [5] S. Kango, R. Sharma, and R. Pandey, "Comparative analysis of textured and grooved hydrodynamic journal bearing," *Proceedings of the Institution of Mechanical Engineers Part J Journal of Engineering Tribology*, vol. 228, no. 1, pp. 82–95, Aug. 2013, doi: [10.1177/1350650113499742](https://doi.org/10.1177/1350650113499742).
- [6] A. Shinde, P. Pawar, P. Shaikh, S. Wangikar, S. Salunkhe, and V. Dhamgaye, "Experimental and Numerical analysis of conical shape Hydrodynamic Journal bearing with partial texturing," *Procedia Manufacturing*, vol. 20, pp. 300–310, Jan. 2018, doi: [10.1016/j.promfg.2018.02.045](https://doi.org/10.1016/j.promfg.2018.02.045).
- [7] B. Manser, I. Belaidi, A. Hamrani, S. Khelladi, and F. Bakir, "Performance of hydrodynamic journal bearing under the combined influence of textured surface and journal misalignment: A numerical survey," *Comptes Rendus Mécanique*, vol. 347, no. 2, pp. 141–165, Jan. 2019, doi: [10.1016/j.crme.2018.11.002](https://doi.org/10.1016/j.crme.2018.11.002).
- [8] S. Cupillard, S. Glavatskih, and M. J. Cervantes, "Computational fluid dynamics analysis of a journal bearing with surface texturing," *Proceedings of the Institution of Mechanical Engineers Part J Journal of Engineering Tribology*, vol. 222, no. 2, pp. 97–107, Feb. 2008, doi: [10.1243/13506501jet319](https://doi.org/10.1243/13506501jet319).
- [9] M. Tauviquirrahman, A. Pratama, J. Jamari, and M. Muchammad, "Hydrodynamic lubrication of textured journal bearing considering slippage: Two-dimensional CFD analysis using multiphase cavitation model," *Tribology in Industry*, vol. 41, no. 3, pp. 401–415, Sep. 2019, doi: [10.24874/ti.2019.41.03.10](https://doi.org/10.24874/ti.2019.41.03.10).
- [10] J. Atwal and R. Pandey, "Performance analysis of thrust pad bearing using micro-rectangular pocket and bionic texture," *Proceedings of the Institution of Mechanical Engineers Part J Journal of Engineering Tribology*, vol. 235, no. 6, pp. 1232–1250, Jul. 2020, doi: [10.1177/1350650120940076](https://doi.org/10.1177/1350650120940076).
- [11] K. Tripathi, B. Joshi, G. Gyawali, A. Amanov, and S. W. Lee, "A study on the effect of laser surface texturing on friction and wear behavior of graphite cast iron," *Journal of Tribology*, vol. 138, no. 1, Jun. 2015, doi: [10.1115/1.4030859](https://doi.org/10.1115/1.4030859).
- [12] S. Wang, Q. Wan, and Z. Xiong, "Stability Analysis of Hydrodynamic Journal Bearing with Surface Texture," *2022 International Conference on Machine Learning and Intelligent Systems Engineering (MLISE)*, pp. 499–502, Jul. 2021, doi: [10.1109/MLISE54096.2021.00104](https://doi.org/10.1109/MLISE54096.2021.00104).
- [13] N. Singh and R. Awasthi, "Influence of dimple location and depth on the performance characteristics of the hydrodynamic journal bearing system," *Proceedings of the Institution of Mechanical Engineers Part J Journal of Engineering Tribology*, vol. 234, no. 9, pp. 1500–

- 1513, Jan. 2020, doi: [10.1177/1350650120901979](https://doi.org/10.1177/1350650120901979).
- [14] S. Sharma, G. Jamwal, and R. K. Awasthi, "Dynamic and stability performance improvement of the hydrodynamic bearing by using triangular-shaped textures," *Proceedings of the Institution of Mechanical Engineers Part J Journal of Engineering Tribology*, vol. 234, no. 9, pp. 1436–1451, Dec. 2019, doi: [10.1177/1350650119891513](https://doi.org/10.1177/1350650119891513).
- [15] F. Meng, Y. Zhang, L. Su, H. Yu, and Y. Zheng, "Dynamic characteristics of compound textured journal bearing," *Proceedings of the Institution of Mechanical Engineers Part J Journal of Engineering Tribology*, vol. 235, no. 7, pp. 1312–1334, Aug. 2020, doi: [10.1177/1350650120951378](https://doi.org/10.1177/1350650120951378).
- [16] S. Matele and K. Pandey, "Effect of surface texturing on the dynamic characteristics of hydrodynamic journal bearing comprising concepts of green tribology," *Proceedings of the Institution of Mechanical Engineers Part J Journal of Engineering Tribology*, vol. 232, no. 11, pp. 1365–1376, Feb. 2018, doi: [10.1177/1350650117752611](https://doi.org/10.1177/1350650117752611).
- [17] D. Sun, S. Li, C. Fei, Y. Ai, and Rhea. P. Liem, "Investigation of the effect of cavitation and journal whirl on static and dynamic characteristics of journal bearing," *Journal of Mechanical Science and Technology*, vol. 33, no. 1, pp. 77–86, Jan. 2019, doi: [10.1007/s12206-018-1208-3](https://doi.org/10.1007/s12206-018-1208-3).
- [18] H. Yamada, H. Taura, and S. Kaneko, "Numerical and experimental analyses of the dynamic characteristics of journal bearings with square dimples," *Journal of Tribology*, vol. 140, no. 1, Jun. 2017, doi: [10.1115/1.4037151](https://doi.org/10.1115/1.4037151).
- [19] B. A. Abass and M. A. A. Muneer, "Static and Dynamic Performance of Journal Bearings lubricated With Nano-Lubricant," *Association of Arab Universities Journal of Engineering Sciences*, vol. 25, no. 2, pp. 201–212, Apr. 2018.
- [20] S. R. Suryawanshi and J. T. Pattiwar, "Experimental study on an influence of bearing geometry and TiO₂ nanoparticle additives on the performance characteristics of fluid film lubricated journal bearing," *Tribology in Industry*, vol. 41, no. 2, pp. 220–236, Jun. 2019, doi: [10.24874/ti.2019.41.02.08](https://doi.org/10.24874/ti.2019.41.02.08).
- [21] T. M. Hammza, "EFFECT OF THE LUBRICANT ADDITIVES ON THE DYNAMIC BEHAVIOUR OF ROTOR BEARING SYSTEMS," *JOURNAL OF MECHANICS OF CONTINUA AND MATHEMATICAL SCIENCES*, vol. 15, no. 3, Mar. 2020, doi: [10.26782/jmcmcs.2020.03.00006](https://doi.org/10.26782/jmcmcs.2020.03.00006).
- [22] H. Awad, K. M. Abdou, and E. Saber, "Steady state characteristics and stability limits of oil lubricated journal bearings using titanium dioxide nanoparticles as lubricant additives," *Results in Engineering*, vol. 20, p. 101486, Oct. 2023, doi: [10.1016/j.rineng.2023.101486](https://doi.org/10.1016/j.rineng.2023.101486).
- [23] F. Rahmani, J. K. Dutt, and R. K. Pandey, "Performance behaviour of elliptical-bore journal bearings lubricated with solid granular particulates," *Particuology*, vol. 27, pp. 51–60, Apr. 2016, doi: [10.1016/j.partic.2015.12.009](https://doi.org/10.1016/j.partic.2015.12.009).
- [24] D. Byotra and S. Sharma, "Performance analysis of textured journal bearing operating with and without nanoparticles in the lubricant," *Industrial Lubrication and Tribology*, vol. 74, no. 9, pp. 1028–1039, Aug. 2022, doi: [10.1108/ilt-03-2022-0078](https://doi.org/10.1108/ilt-03-2022-0078).
- [25] D. Byotra and S. Sharma, "Effect of texture shapes and additives in lubricants on the dynamic characteristics of the hydrodynamic journal bearing," *Industrial Lubrication and Tribology*, vol. 75, no. 9, pp. 1031–1044, Sep. 2023, doi: [10.1108/ilt-06-2023-0178](https://doi.org/10.1108/ilt-06-2023-0178).
- [26] H. Yin, X. Zhang, Z. Guo, Y. Xu, X. Rao, and C. Yuan, "Synergetic effects of surface textures with modified copper nanoparticles lubricant additives on the tribological properties of cylinder liner-piston ring," *Tribology International*, vol. 178, p. 108085, Nov. 2022, doi: [10.1016/j.triboint.2022.108085](https://doi.org/10.1016/j.triboint.2022.108085).
- [27] M. B. Dobrica and M. Fillon, "About the validity of Reynolds equation and inertia effects in textured sliders of infinite width," *Proceedings of the Institution of Mechanical Engineers Part J Journal of Engineering Tribology*, vol. 223, no. 1, pp. 69–78, Dec. 2008, doi: [10.1243/13506501jet433](https://doi.org/10.1243/13506501jet433).
- [28] ANSYS Inc., *ANSYS Fluent Theory Guide*, Release 2021 R2. Canonsburg, PA: ANSYS Inc., 2021. [E-book] Available: ANSYS Customer Portal.
- [29] D. Y. Dhande and D. W. Pande, "Numerical analysis of multiphase flow in hydrodynamic journal bearing using CFD coupled fluid-structure interaction with cavitation," in *International Conference on Automatic Control and Dynamic Optimization Techniques (ICACDOT)*, Pune, India, Sep. 9–10, 2016, pp. 964–971, doi: [10.1109/ICACDOT.2016.7877731](https://doi.org/10.1109/ICACDOT.2016.7877731).
- [30] M. O. Yasir, S. Y. Ahmed, and B. A. Abass, "Performance analysis of experimentally characterized titanium dioxide and zinc oxide Nano-Lubricated Journal bearing considering thermal and cavitation effects," *Arabian Journal for Science and Engineering*, vol. 48, no. 3, pp. 3599–3614, Sep. 2022, doi: [10.1007/s13369-022-07219-0](https://doi.org/10.1007/s13369-022-07219-0).

- [31] I. M. Krieger and T. J. Dougherty, "A mechanism for Non-Newtonian flow in suspensions of rigid spheres," *Transactions of the Society of Rheology*, vol. 3, no. 1, pp. 137–152, Mar. 1959, doi: [10.1122/1.548848](https://doi.org/10.1122/1.548848).
- [32] I. M. Mahbubul, R. Saidur, and M. A. Amalina, "Latest developments on the viscosity of nanofluids," *International Journal of Heat and Mass Transfer*, vol. 55, no. 4, pp. 874–885, Oct. 2011, doi: [10.1016/j.ijheatmasstransfer.2011.10.021](https://doi.org/10.1016/j.ijheatmasstransfer.2011.10.021).
- [33] M. Kole and T. K. Dey, "Effect of aggregation on the viscosity of copper oxide-gear oil nanofluids," *International Journal of Thermal Sciences*, vol. 50, no. 9, pp. 1741–1747, May 2011, doi: [10.1016/j.ijthermalsci.2011.03.027](https://doi.org/10.1016/j.ijthermalsci.2011.03.027).
- [34] H. Chen, Y. Ding, and C. Tan, "Rheological behaviour of nanofluids," *New Journal of Physics*, vol. 9, no. 10, p. 367, Oct. 2007, doi: [10.1088/1367-2630/9/10/367](https://doi.org/10.1088/1367-2630/9/10/367).
- [35] K. G. Binu, B. S. Shenoy, D. S. Rao, and R. Pai, "A Variable Viscosity Approach for the Evaluation of Load Carrying Capacity of Oil Lubricated Journal Bearing with TiO₂ Nanoparticles as Lubricant Additives," *Procedia Materials Science*, vol. 6, pp. 1051–1067, Jan. 2014, doi: [10.1016/j.mspro.2014.07.176](https://doi.org/10.1016/j.mspro.2014.07.176).
- [36] B. Maneshian and S. a G. Nassab, "Thermohydrodynamic analysis of turbulent flow in journal bearings running under different steady conditions," *Proceedings of the Institution of Mechanical Engineers Part J Journal of Engineering Tribology*, vol. 223, no. 8, pp. 1115–1127, Mar. 2009, doi: [10.1243/13506501jet575](https://doi.org/10.1243/13506501jet575).
- [37] T. N. Jaber, K. A. Sukkar, and A. A. Karamalluh, "Specifications of heavy diesel lubricating oil improved by MWCNTs and CUO as nano-additives," in 1st International Conference on Petroleum Technology and Petrochemicals, *IOP Conference Series Materials Science and Engineering*, vol. 579, no. 1, p. 012014, Jul. 2019, doi: [10.1088/1757-899x/579/1/012014](https://doi.org/10.1088/1757-899x/579/1/012014).
- [38] W. H. Azmi, K. V. Sharma, P. K. Sarma, R. Mamat, S. Anuar, and V. D. Rao, "Experimental determination of turbulent forced convection heat transfer and friction factor with SiO₂ nanofluid," *Experimental Thermal and Fluid Science*, vol. 51, pp. 103–111, Jul. 2013, doi: [10.1016/j.expthermflusci.2013.07.006](https://doi.org/10.1016/j.expthermflusci.2013.07.006).
- [39] X. Liang, X. Yan, Z. Liu, and W. Ouyang, "Effect of perturbation amplitudes on water film stiffness coefficients of water-lubricated plain journal bearings based on CFD-FSI methods," *Proceedings of the Institution of Mechanical Engineers Part J Journal of Engineering Tribology*, vol. 233, no. 7, pp. 1003–1015, Dec. 2018, doi: [10.1177/1350650118818027](https://doi.org/10.1177/1350650118818027).
- [40] F. Hemmati, M. Miraskari, and M. S. Gadala, "Dynamic analysis of short and long journal bearings in laminar and turbulent regimes, application in critical shaft stiffness determination," *Applied Mathematical Modelling*, vol. 48, pp. 451–475, Apr. 2017, doi: [10.1016/j.apm.2017.04.013](https://doi.org/10.1016/j.apm.2017.04.013).
- [41] M. R. Hameed, S. A. Ali, H. H. Hadwan, A. A. Toman, and M. A. Mahdi, "Cfd-fsi analysis of textured journal bearing working with nano lubricant," *Diagnostyka*, vol. 25, no. 2, pp. 1–10, May 2024, doi: [10.29354/diag/188391](https://doi.org/10.29354/diag/188391).
- [42] P. Li, F. Zeng, S. Xiao, D. Zhen, H. Zhang, and Z. Shi, "Effects of texture bottom profile on static and dynamic characteristics of journal bearings," *Shock and Vibration*, vol. 2021, no. 1, Jan. 2021, doi: [10.1155/2021/7068744](https://doi.org/10.1155/2021/7068744).
- [43] C. B. Khatri and S. C. Sharma, "Influence of textured surface on the performance of non-recessed hybrid journal bearing operating with non-Newtonian lubricant," *Tribology International*, vol. 95, pp. 221–235, Dec. 2015, doi: [10.1016/j.triboint.2015.11.017](https://doi.org/10.1016/j.triboint.2015.11.017).
- [44] S. Kango, R. K. Sharma, and R. K. Pandey, "Thermal analysis of microtextured journal bearing using non-Newtonian rheology of lubricant and JFO boundary conditions," *Tribology International*, vol. 69, pp. 19–29, Aug. 2013, doi: [10.1016/j.triboint.2013.08.009](https://doi.org/10.1016/j.triboint.2013.08.009).
- [45] D. Byotra and S. Sharma, "Dynamic and stability analysis of crescent geometry-possessing textured journal bearing using nanolubricant," *Industrial Lubrication and Tribology*, vol. 76, no. 6, pp. 788–803, Jun. 2024, doi: [10.1108/ilt-03-2024-0089](https://doi.org/10.1108/ilt-03-2024-0089).
- [46] F. Ilie and C. Covaliu, "Tribological properties of the lubricant containing titanium dioxide nanoparticles as an additive," *Lubricants*, vol. 4, no. 2, p. 12, Apr. 2016, doi: [10.3390/lubricants4020012](https://doi.org/10.3390/lubricants4020012).
- [47] S. B. Kalakada, P. N. N. Kumarapillai, and K. P. K. Rajendra, "Static characteristics of thermohydrodynamic journal bearing operating under lubricants containing nanoparticles," *Industrial Lubrication and Tribology*, vol. 67, no. 1, pp. 38–46, Feb. 2015, doi: [10.1108/ilt-01-2013-0015](https://doi.org/10.1108/ilt-01-2013-0015).